Controlling facets and defects of InP nanostructures in confined epitaxial lateral overgrowth

Aranya Goswami [1], Simone T. Šuran Brunelli [1], Brian Markman [1], Aidan A. Taylor [2], Hsin-Ying Tseng [1], Kunal Mukherjee [2], Mark Rodwell [1], Jonathan Klamkin [1], and Chris J. Palmstrøm [1,2,3,*]

[1] Electrical and Computer Engineering Department, University of California Santa Barbara, Santa Barbara, California 93106, USA
[2] Materials Department, University of California Santa Barbara, Santa Barbara, California 93106, USA
[3] California NanoSystems Institute, University of California Santa Barbara, Santa Barbara, California 93106, USA

(Received 20 July 2020; accepted 10 November 2020; published 9 December 2020)

The selective area growth technique, confined epitaxial lateral overgrowth (CELO), enables the growth of lateral III-V heterojunctions integrated on mismatched substrates. In CELO, effective control of facet shapes, as well as defect-free growths are essential to fabricating high-quality nanostructures with custom geometries. Here, the effects of growth temperature, V/III ratio, template alignments, and substrate orientations on the observed facets and defect densities in CELO grown InP and related materials on InP substrates are investigated. The nanostructure facets and defects are determined using a combination of plan-view and cross-sectional transmission electron microscopy. For homoepitaxial CELO growth on InP (100) substrates, growth temperatures below 575 °C, and high V/III ratios of 450 aid in increasing the surface areas of the $\{111\}B$ facets, while reducing defect densities. Further, by changing template alignments, the effective areas of overgrowth can be tuned, and defects can be lowered, with templates aligned along $[0\bar{1}0]$ yielding the largest defect-free areas. By aligning templates in the $[\bar{1}10]$ orientation on a (110) InP substrate, near defect-free overgrowth with perfectly flat perpendicular single $(1\bar{1}\,0)$ facets can be achieved. This is an essential feature to enable the growth of lateral III-V heterojunctions, as is demonstrated by growing InP/InGaAs CELO heterojunctions with $\{110\}$ facets.

DOI: 10.1103/PhysRevMaterials.4.123403

I. INTRODUCTION

The III-V compound semiconductor materials have a low electron effective mass and a direct band gap, making them ideal for high-speed electronic and photonic devices. Power-efficient electronic devices using triple heterojunction III-V tunnel field effect transistors [1,2] have been proposed. Carrier confinement combined with crystallographic anisotropies in the energy bands of III-V materials can be used to increase on-state currents, reduce leakage currents and improve switching behavior in these devices. Device geometry and dimensions play a significant role in achieving such superior performances, where fins, less than 100 nm thick, are often required to confine carriers. To be able to fabricate such devices and make them industrially compatible, we need the capability to grow high-quality III-V nanostructures with low defect densities and integrate them on a variety of substrates. However, etching-induced defects in fins fabricated from vertical epitaxy might degrade device performance [3,4], and alignment of vertical gates to these fins is difficult. Large-scale integration of nanoscale devices on mismatched substrates is also challenging. A wide variety of techniques have been explored, including direct wafer bonding and heteroepitaxy [5]. Most of these techniques suffer from defects in the final integrated III-V layer. These include bonding defects in direct wafer bonding [6], as well as misfit dislocations and antiphase boundaries in heteroepitaxially grown III-V layers on Si [7]. In response to these challenges, confined epitaxial lateral overgrowth (CELO) offers scalable fabrication and potentially defect-free integration of in-plane devices of custom geometries at lithographically defined positions on the chip.

First developed for fabricating silicon-on-insulator substrates [8,9], CELO has been adapted for III-V epitaxy on Si [10–16] to produce advanced semiconductor devices, such as GaSb/InAs tunnel transistors [17], InGaAs metal-oxide-semiconductor field-effect transistors (MOSFETs) on Si [18], and microdisk lasers of GaAs or InP [7,19]. CELO uses a patterned, oxide-covered substrate with “seed holes” etched down to the substrate, where III-V material is grown selectively. Prefabricated templates confine and direct the epitaxial growth laterally towards a defined direction on the oxide. Thus, CELO results in growth of materials in predefined shapes eliminating the need for several postgrowth processing steps. The dielectric boundaries at the seed hole limit propagation of the defects arising from lattice mismatch [see Fig. 1(a)]. Since the growth proceeds outwards from a seed hole, CELO also allows the growth of lateral heterojunctions [17,20]. Flat facets perpendicular to the growth direction can offer single confinement planes and improved performance of lateral quantum wells [Fig. 1(a.ii)]. Therefore, the ability to efficiently control the final facet shapes in CELO is crucial for fabricating lateral heterojunction-based devices [1,2,21].The ability to fabricate planar gates to electrostatically control such lateral heterojunctions vastly increases flexibility in fabricating heterojunction-based devices using CELO.

In spite of the techniques’ promise, growing completely defect-free nanostructures with well-controlled facets is challenging with CELO. CELO grown nanostructures tend to suffer from high densities of extended defects, such as

*cjpalm@ucsb.edu

 ©2020 American Physical Society

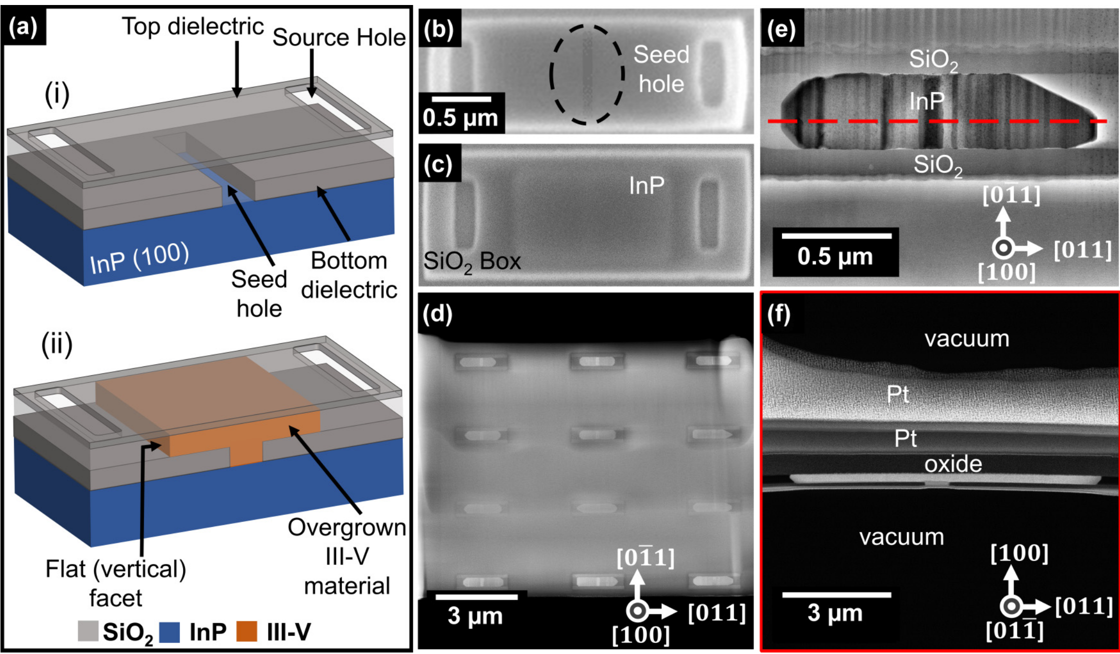

FIG. 1. (a) Schematic of CELO template before growth (a.i) and after III-V overgrowth (a.ii) (b), (c), respectively, show top-down scanning electron microscopy images of a CELO template before growth and after InP overgrowth. (d) High-angle annular dark field (HAADF) STEM of a plan-view lamella containing CELO structures post-InP growth. (e) Plan-view bright field STEM image of a CELO template with grown InP inside it. The light and dark contrast corresponds to regions with and without defects. (f) Cross-section HAADF STEM from the plan-view sample (e) along the red dashed line. See Methods for details on each technique.

rotational twins and stacking faults (SFs) [14,16]. This problem is especially prominent in materials like InP, which have low stacking fault energies [22–24]. Defects introduce nonradiative recombination centers and scattering planes [16], thus lowering performance by increasing leakage currents and reducing quantum efficiency, carrier lifetime, and mobility. Therefore, reducing defect densities in CELO nanostructures is important for fabricating efficient devices.

The impact of growth conditions, substrate orientations, and template geometries on the facet shapes and defect densities is poorly understood in the widely used InP system. Because growth of InP on Si introduces interfacial defects due to lattice and symmetry mismatch, here we study homoepitaxial CELO growth on InP substrates to isolate the fundamental variables controlling InP CELO itself. The results from this study can be extended to other heteroepitaxial CELO systems. In this work, we report on the conditions of substrate temperature and V/III ratio that are found to control the ratio of the $\{111\}B$ to $\{110\}$ facets in CELO on the InP (100) substrate. We show how a low-temperature growth coupled with [100] template alignments can effectively reduce defect densities. Facets and the three-dimensional distribution and alignment of extended defects in the CELO nanostructures are comprehensively analyzed. For this purpose, a combination of plan-view and cross-sectional scanning transmission electron microscopy (STEM) on the same structure has been used to characterize individual CELO overgrowths [Figs. 1(d)–1(f)]. Finally, applying our observations of growth conditions on (100) substrates, we demonstrate CELO on a (110) InP substrate to achieve defect-free overgrowths of InP and InP/InGaAs heterojunctions with perpendicular flat facets, a feature important for the future development of lateral epitaxial heterojunction devices.

II. EXPERIMENT

A. Template fabrication methods and material growth

Templates of varying sizes were fabricated on InP (100) and InP (110) 2-in. *n*-type AXT wafers. The process begins with an atomic layer deposited (ALD) 3-nm-thick alumina etch stop layer followed by a plasma enhanced chemical vapor deposition (PECVD) grown SiO_2 layer, approximately 30 nm thick. Openings with dimensions of $100\,nm \times 1\,\mu m$ in the SiO_2 layer were then patterned by electron beam lithography (EBL) and etched by inductively coupled plasma (ICP) using $CHF_3/CF_4/O_2$ chemistry, thus defining the seed, where growth will selectively initiate. Following this, a sacrificial layer of amorphous Si approximately 50 nm thick was sputter deposited and then patterned to define the area that will become the growth cavity. A 100-nm top dielectric of PECVD SiO_2 was then deposited and patterned, exposing the sacrificial region, which in turn is selectively removed via a XeF_2 dry etch. Processed wafers were diced into $7 \times 7\,mm^2$ samples, each containing four die. Finally, tetra methyl ammonium hydroxide (TMAH) is used to remove the alumina etch stop layer exposing the seed, followed by a diluted HF dip. Fabrication steps are shown in detail in Fig. S9 of the Supplemental Material (SM) [25]. Metal organic chemical vapor deposition (MOCVD) growth of InP was performed in a horizontal reactor using trimethylindium (TMIn) and tertiarybutylphosphine (TBP) with H_2 as the carrier gas. The growth temperature was varied from 550 °C to 630 °C, as measured

with a thermocouple at the susceptor. TMIn flow rate was set to 25 SCCM (cubic centimeter per minute at STP) for the initial 500 s of growth, then increased according to the V/III required for the particular growth. An *in situ* anneal was conducted before growth and consisted of two steps: 350 °C for 10 min in a hydrogen atmosphere, followed by 10 min at 660 °C under both hydrogen and TBP to avoid group-V desorption from the InP surface.

B. SEM characterization

Top-down scanning electron microscopy (SEM) was performed using a FEI Nova Nano 650 field emission gun (FEG) SEM to determine the area of growth in the templates and provide an initial estimate of crystal quality. The top oxide is thin enough to allow for secondary electron emission contrast in the SEM between the grown film and an empty cavity [Fig. 1(c)]. SEM also provides a rough indication of the facet types. The backscatter electron detector was used to obtain atomic number contrast (Z contrast) images.

C. TEM lamella preparation and imaging

Cross-sectional transmission electron microscopy (TEM) samples were made using a standard lift-out technique in a FEI Helios Dualbeam Nanolab 600 Focused Ion Beam (FIB) system [26]. To prepare the plan-view TEM samples from a particular region of the sample containing the templates, a modified technique based on Li *et al.* is followed [27]. A wedge-shaped area containing the templates was lifted out from the surface of the sample using a FIB and thereafter thinned from the back using the FIB until it was electron transparent. This technique allowed site specific wide area ($11\,\mu$m $\times$ $10\,\mu$m) electron transparent lamellas which were around 200 nm thick and could accommodate a 3×4 array of the CELO templates [Fig. 1(d)] thus giving results from multiple CELO grown structures from a single TEM lamella.

After complete TEM analysis of the plan-view samples, the plan-view lamella was put back into the FIB to make a cross-section sample out of a specific region of the lamella. The area of interest on the plan-view lamella was protected by *in situ* deposited Pt, lifted out and subsequently thinned down in steps. Care was taken to keep the incident beam angle of the lamella against the ion beam relatively low (less than 2°, unlike conventional cross-sectional TEM lamella thinning) to prevent damaging the region of interest at the bottom 100 nm of the lamella. Thus, a cross-sectional sample from a plan-view sample can be achieved. One of the advantages of this method is that multiple such cross-sectional samples can be prepared from the same plan-view lamella if they are sufficiently far apart. This is therefore a fast feedback method applicable to characterizing other nanostructures as well. A schematic of lamella preparation methods and details of the process are described in the Supplemental Material [25].

The plan-view lamellas were inspected and analyzed in a FEI Titan 80–300 kV FEG TEM STEM using the scanning TEM (STEM) mode at 300 kV. The high beam current makes sure that a considerable signal can be achieved from a relatively thick sample with a convergent beam. For the bright field (BF) STEM images, the sample was aligned to a zone axis and a 50-μm objective aperture was used to select the central transmitted beam. This is a particularly useful technique to study defects and dislocations in thicker TEM samples [28,29].

High-angle annular dark field (HAADF) STEM images are also acquired for the same structures to inspect any variation of chemical composition using Z (atomic number) contrast. The cross-sectional lamellas made from the plan-view lamellas further corroborate this information. Dark field (DF) TEM and HAADF STEM on these cross-sectional samples are used to correlate the defects and dislocations observed in plan-view imaging with cross-sectional data. By using a combination of plan-view STEM, cross-sectional dark field TEM, and cross-sectional STEM of the CELO templates, a complete picture of the facets and defects can be achieved.

III. RESULTS

A. Effects of growth temperature on facets of InP CELO on (100) InP substrate

To understand the effects of growth temperature on the evolution of facets in CELO nanostructures, the growths were done at four different temperatures of 630 °C, 600 °C, 570 °C, and 550 °C. The growths were performed on a (100) InP substrate in a metalorganic chemical vapor deposition (MOCVD) chamber using a V/III (TBP/TMIn) ratio of 450. Plan-view STEM is used to characterize the facets and defects in these structures (Fig. 2). It was observed that the high-temperature growths (630 °C and 600 °C) exhibit two {110} type side facets which form 45° angles to the template direction (along $[0\bar{1}\bar{1}]$), along with a {111} facet forming a 90° angle to the template direction [Figs. 2(a) and 2(b)]. The low-temperature growths (570 °C and 550 °C) result in predominantly rectangular shaped overgrowths with {111} facets [Figs. 2(c) and 2(d)] at an angle of 90° to the template direction. To further assess the structural quality of these crystals, we performed cross-sectional STEM on the plan-view STEM lamellas.

To understand the exact orientation of the end facets, we looked at both the plan-view and cross-sectional STEM of a CELO nanostructure, grown at 600 °C (Fig. 3). In this high-temperature growth mode, large {110} type facets (marked by red dotted lines) appear in combination with {111} facets. Cross-sectional STEM reveals that the left end of the overgrowth shows a combination of small $(1\bar{1}\bar{1})A$ and large $(\overline{211})B$ facets [Fig. 3(d)] and a combination of $\{111\}B$ and {110} facets [Fig. 3(c)] on the right end. Cross-sectional STEM images confirm the side facets to be {110} type (Fig. S5 in the SM [25]). The structures also occasionally show the appearance of other higher-order facets, such as (113) [Fig. 3(b)]. Thus, at high temperatures, we observe a combination of {110} and {111} (mostly B type) facets.

We then examine the facets in low-temperature growth by performing STEM analysis on a CELO sample grown at 570 °C (Fig. 4). The plan-view STEM [Fig. 4(a)] and its cross-section [Figs. 4(b)–4(d)] images show that the end facets in this case are primarily $\{111\}B$ type facets with only a small fraction of {110} type facets. Both ends of the overgrown structure show the same facet combinations. At 45° to the

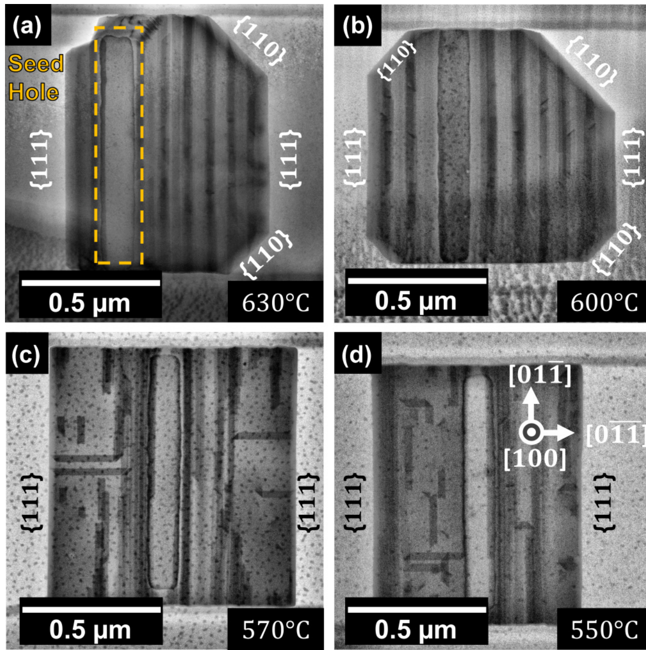

FIG. 2. BF STEM plan-view images of InP CELO grown on (100) InP substrates at different growth temperatures of (a) 630 °C, (b) 600 °C, (c) 570 °C, and (d) 550 °C. The samples (a), (b) grown at higher temperatures show {110} type side facets and {111} type end facets (plan-view STEM cannot distinguish between, for instance, $(1\bar{1}0)$ and $(\bar{1}\bar{1}0)$ or between $(1\bar{1}\bar{1})A$ and $(\bar{1}\bar{1}\bar{1})B$. Hence, {110} or {111} is used). The samples (c), (d) grown at lower temperatures show rectangular overgrowths with primarily {111} type end facets. The orientation of all the samples is the same [as shown in (d)] and the direction of the template is along $[0\bar{1}\bar{1}]$.

direction of the template, the {110} facets either do not appear, or are very small. Therefore at low-temperature growths we can effectively eliminate any side facets and have a single growth front composed of {110} and {111}*B* facets.

Thus these result show that the growth temperature plays an important role in tuning the ratio of the {111}*B* to the {110} facets in the CELO nanostructures grown on (100) InP substrates.

B. Effects of growth temperature on defects of InP CELO on (100) InP substrate

To understand the impact of growth temperature on defect formation, we again analyze the STEM micrographs to map the position and orientation of the defects. The light and dark contrasts in plan-view STEMs provide crucial information on the crystal quality. For example, in a crystal aligned to a major zone axis, such as [110], areas of high crystalline quality are expected to appear relatively dark in bright field (BF) STEM. This is due to the high probability of the incident beam electrons being diffracted by one of the many sets of planes close to their Bragg diffraction condition, and subsequently getting blocked by the objective aperture in a BF mode [28,29]. Conversely, areas that have a high concentration of stacking faults and planar defects will appear lighter. This is due to the lower interaction cross section of the incident beam with these areas of reduced long-range crystalline order.

In the samples grown at high temperature [Figs. 2(a), 2(b), 3(a), and 3(b)], we observe alternate bands of light and dark contrast in the plan-view TEM image—indicating areas with and without defects. In Fig. 3(a), the white arrows marked 1 and 2 correspond to regions with low density of defects (hence darker), while arrow 3 points to a region with a high density of stacking faults (hence lighter). Dark field cross-sectional TEM images confirm this result (Fig. S4 in the SM [25]). HR STEM [Fig. 3(e)] images collected from the cross section along red dashed line in Fig. 3(a) confirm that the bands of dark contrast [Figs. 3(a) and 3(e), green shaded part of yellow box] are areas of pure zinc-blende InP crystal with no defects. Neighboring areas [Figs. 3(a) and 3(e), red shaded parts of yellow box] with stacking faults or a mix of zinc-blende and wurtzite crystal phases appear as lighter contrast in the plan-view STEM image. The brightness of these lighter regions full of stacking faults or mixed phases roughly correlates to the density of defects. The width of the alternating dark and light bands are uniform over CELO structures from the same sample. Thus, at high temperatures we observe areas of the overgrowth exhibiting a high density of stacking faults in between areas of crystals with no defects.

When grown at a lower temperature (570 °C), the CELO samples have far fewer defects compared to the high-temperature grown samples (Fig. 4). Notably, large areas of the crystal appear completely free of planar defects. However, we observe some stacking faults, which appear as darker trapezoids intersecting each other perpendicularly throughout the whole crystal. The stacking faults are in the {111}*B* planes and perpendicularly intersect, possibly along a line dislocation [Fig. 4(e)]. Isolated stacking faults also appear, bounded on both sides by partial dislocations. The high-resolution cross-sectional STEM taken on the lamella cut along the red dashed line [Figs. 4(a)–4(c)] confirms the presence of these stacking faults along the {111}*B* planes. Thus, low-temperature growths show nanostructures with significantly fewer defects than for the high-temperature growths.

Growth temperature is therefore an important control knob to lower the density of defects observed in these CELO grown structures.

C. Effects of P/In ratio for CELO on a (100) InP substrate

Surface energies of facets and growth rates are often dependent on the V/III ratio during growth and can significantly control final facet morphologies in CELO. Therefore, we explore the impact of V/III ratios during growth in controlling facets and defects of InP CELO nanostructures. For this, two InP CELO samples were grown at 570 °C at two different V/III ratios of 450 and 225, by adjusting the group-V flux and keeping the group-III flow fixed at 4×10^{-6}mol/min. Overgrowths containing {111} type end facets [Fig. 5(b)] were predominantly observed in the higher V/III ratio growth. The lower V/III ratio growth, on the other hand, yields a higher percentage of {110} facets, which are at 45° to the template direction [Fig. 5(d)]. Comparing dependence of growths on temperature (Fig. 2) and V/III ratios (Fig. 5), we observe that high V/III ratio [Fig. 5(b)] and low temperature [Figs. 2(c) and 2(d)] have similar facets and defects. Samples grown at low V/III ratio [Fig. 5(d)] and high temperature [Figs. 2(a)

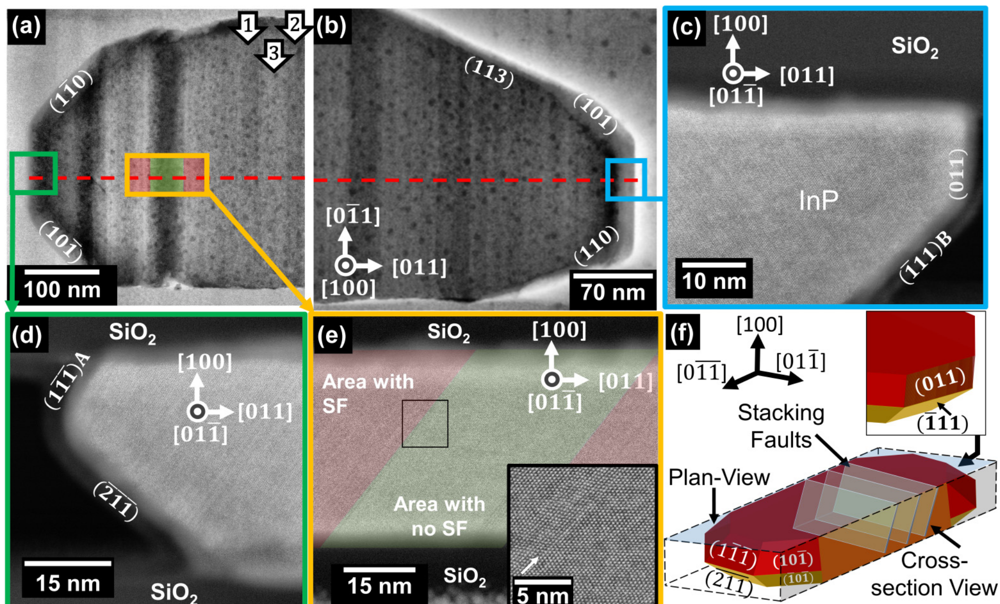

FIG. 3. InP CELO grown on (100) InP at 600 °C. (a) BF STEM image of the plan-view sample showing defective (light) and nondefective (dark) areas. White arrows (1,2) point to two relatively defect-free areas, arrow 3 points to a defect-dense area. (b) Shows the plan-view BF STEM of the other end of the same growth. (c) HAADF STEM of cross section taken along red line in (b) showing a (011) and a $(\bar{1}11)B$ facet. (d) Cross-section STEM of the plan-view lamella in (a) taken along the red dashed line showing $(1\overline{11})A$ and $(\overline{211})B$ end facets. (e) STEM corresponding to the area marked by the yellow box in (a) showing a defect-free region (green) in between areas with high densities of SFs and twins (red). Inset shows a high-resolution STEM of the region marked by the black square. White arrow points to a stacking fault. (f) Three-dimensional (3D) visualization of the facets in this overgrowth.

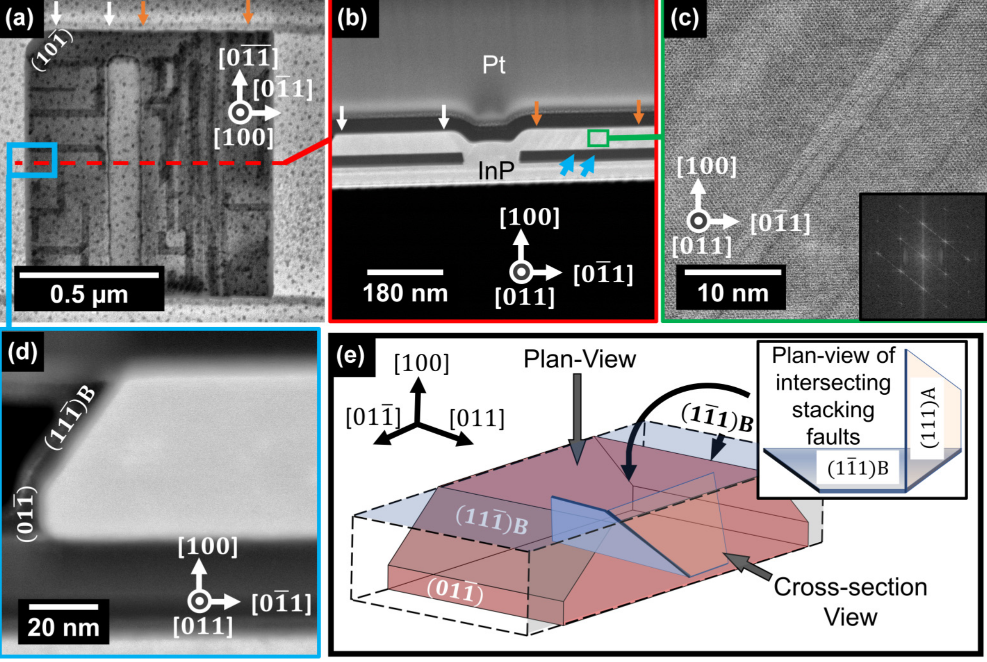

FIG. 4. InP CELO on InP (100) substrates grown at 570 °C. (a) BF STEM of a CELO structure showing defects as dark contrasts. (b) shows HAADF STEM of a cross-sectional cut taken along red dashed line in (a). In (a), (b) orange and white arrows show limits of defective and defect-free regions, respectively. Blue arrow marks SFs in the defective part. (c) shows a high-resolution cross-section STEM of the region marked by a blue box in (b). Inset shows Fourier transform with the streaks along [111] corresponding to the SFs. (d) shows cross-sectional STEM of the end facet marked by the blue box in (a). (e) shows a 3D visualization of the facets and orientation of the intersecting stacking fault planes. The inset shows the pair of intersecting SFs as seen when looking along the top gray arrow (plan view).

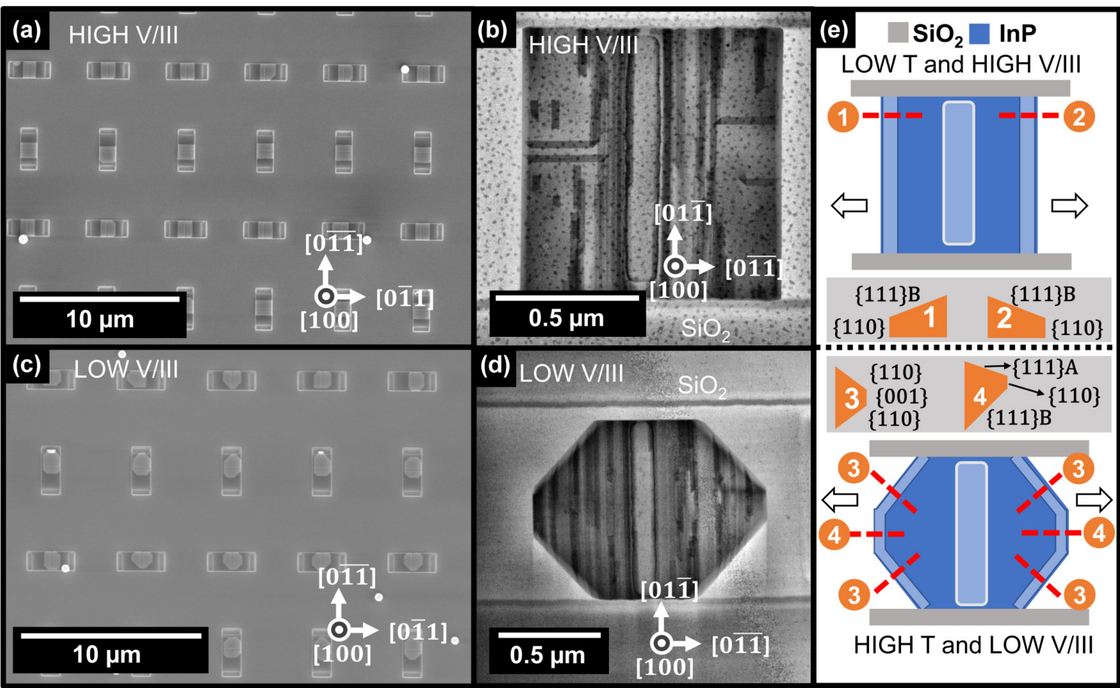

FIG. 5. InP CELO growths on (100) InP substrate at 570 °C with different V/III ratios. (a), (b) show the top-view SEM (of a region with multiple CELO templates) and BF STEM of a representative structure, respectively, for a growth done at a high V/III ratio of 700. (c), (d) show the top-view SEM (of regions with multiple CELO templates) and BF STEM of a representative structure, respectively, for a growth done at low V/III ratio of 240. The scale bars in (a), (c) are both 10 μm. (e) shows a schematic top-down view representation of the change in faceting with temperature and V/III ratio. The insets show cross-section schematics of the facets observed, where the relative ratio of the facets varies. The arrows in (e) point to the growth direction out of the center seed hole.

and 2(b)] also show similar facets and defects. Therefore, similar to temperature, V/III ratio gives us a second control knob in tuning the facets and defects in CELO grown InP nanostructures. In effect, by changing temperature or V/III ratios we can adjust the relative stabilities or growth rates of different facets.

D. Influence of template orientation for CELO on (100) InP substrate

To examine the effects of growing along different template orientations, we fabricate CELO templates along different directions at 18° intervals away from the [011] [Fig. 6(a)]. We grew at 570 °C because this temperature previously led to lower defect density (Fig 2). From the previous results (Fig. 4), a low-temperature growth should result in a higher fraction of $\{111\}B$ type facets compared to {110} facets in the final structures. This is confirmed by the plan-view BF STEM (Fig. 6). The growths in the templates oriented along the [010] direction show regions with the largest area of defect-free overgrown crystal [Fig. 6(b)]. Stacking faults form along the edges, parallel to the {110} side facets. The total area of the growth varies with the orientation of the templates [Fig. 6(g)], decreasing from the maximum in templates aligned along $[0\bar{1}0]$ to a minimum for templates along $[0\bar{1}1]$, and then increasing again. Similarly, as the direction of the template changes from being oriented along $[0\ \bar{1}\ 0]$ [Fig. 6(b)] to being oriented along $[0\ \bar{1}\ 1]$, the area of defect-free crystal decreases and stacking faults increase throughout the crystal [Fig. 6(e)]. This is illustrated in the plot of Fig. 6(h). Note that the stacking faults appear to be nucleated at the mask sidewalls suggesting that optimal template orientations can be used to design CELO overgrowths with a lower density of defects.

E. CELO on a (110) InP substrate

For fabricating lateral heterojunction-based devices, heterojunctions with single facets perpendicular to the lateral growth direction of the template are optimal [1,2,21]. From our study of growth on (100) InP substrates, the ratios of the {110} and {111} facets can be adjusted using temperature and V/III ratio. This suggests that changing the substrate orientation and choosing the correct template alignments might enable the {111} or {110} surfaces to form the desirable perpendicular flat facet structures. A (110) substrate can potentially allow the formation of this perpendicular {110} facet, since {111} planes are absent in the $[\bar{1}10]$ direction of growth. Therefore, we explored CELO growths on a (110) type InP substrate as a possible route to achieving these vertical facets. The templates examined here are oriented either towards [001] or $[\bar{1}10]$. This orientation on the (110) InP substrate is crucial, since unlike the (100) substrate the mutually perpendicular [001] and $[\bar{1}10]$ growth directions offer asymmetric crystallographic planes to grow on. As a result, the growths in these perpendicular templates will be different and need to be explored separately. In addition, we grew InP CELO samples in these templates with thin lattice matched InGaAs spacer marker layers, added after constant growth time intervals of InP growth. The InGaAs markers are easily identifiable in

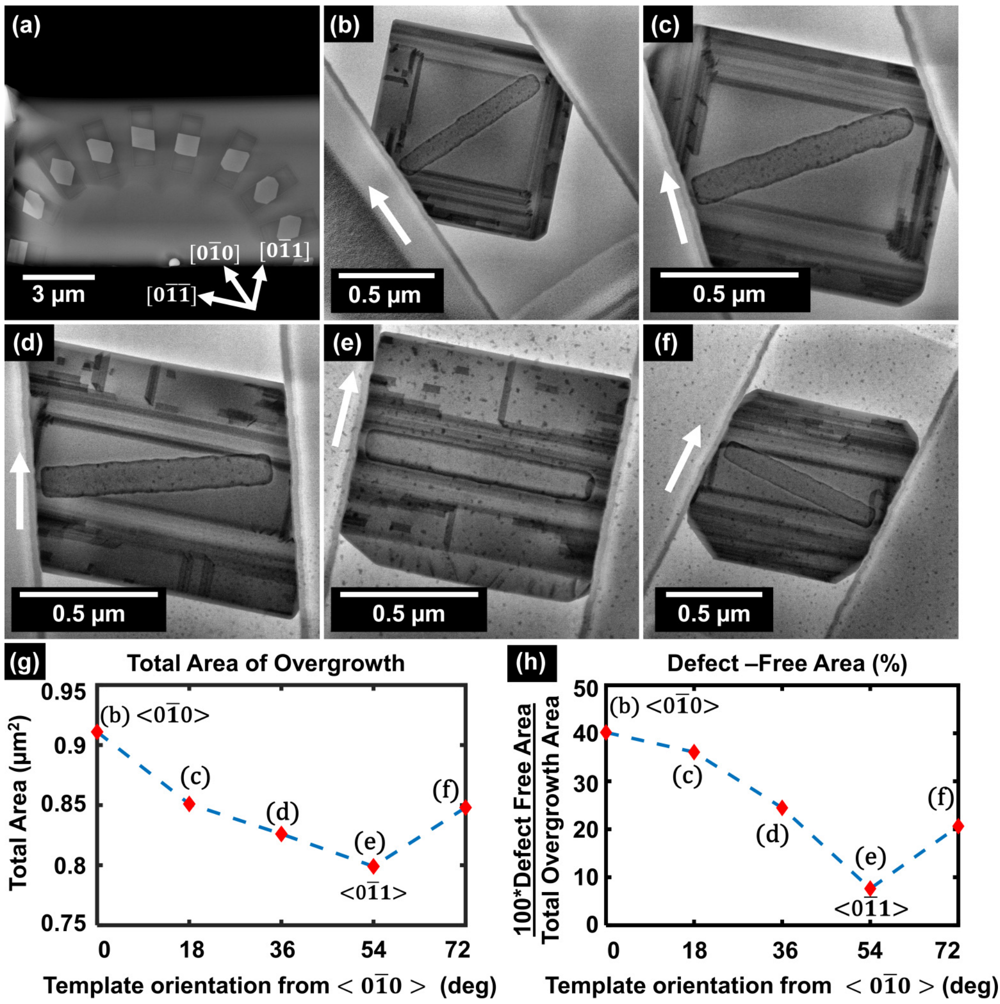

FIG. 6. Plan-view TEM micrographs analyzing growth in different orientations on a (100) InP substrate. (a) shows the HAADF STEM of the entire lamella with a flower pattern of CELO templates starting from the one oriented along [110] and with separations of 18° between consecutive templates. (b)–(f) BF STEM of individual templates oriented in different directions on the wafer. The nature and density of defects change as the orientations of the templates vary from [0 $\bar{1}\bar{1}$] to [0 $\bar{1}$1]. The white arrows point to the direction that the templates are oriented. (g) shows the total area of overgrown III-V materials in each of these templates and (h) shows the fraction of defect-free area in the different samples.

STEM due to Z contrast and help elucidate the progress of the growth front from the start of the growth to the final facets. The facet shapes remain unchanged with the introduction of the InGaAs layer.

In the (110) growths we observed tunability of final facets in overgrowths using template orientation, ultimately leading to a defect-free overgrowth with perfect flat facets. A large number of growths in the templates directed along [$\bar{1}$10] are twinned along $\{111\}A$ [red dashed lines, Fig. 7(a)]. A combination of $\{111\}A$, $\{112\}$, and $\{111\}B$ facets terminate the growth along with the formation of twins. Comparing the total length of growth in each orientation, the growth rates appear higher on $\{111\}A$ compared to $\{111\}B$ [Fig. 7(a)]. The initial portion of the crystal growth close to the seed hole contains no defects, until the formation of the twin. The twinned part of the crystal has a high density of stacking faults. Occasionally we also found a small number of stacking faults running along the direction of growth. The most striking observation in these CELO growths on (110) InP substrates is the formation of flat $\{\bar{1}10\}$ vertical facets in the templates oriented along [$\bar{1}$10] [Fig. 7(b)]. Such growths have a perfect rectangular shape and appear to show no defects from the plan-view STEM studies. The yield of such nanostructures is about 20%. InGaAs spacer layers lattice matched to InP were introduced to track the evolution of growths in the lateral overgrowths in such [$\bar{1}$10] oriented templates [Fig. 7(d)]. Top-view SEM backscatter images show that in the structures that result in $\{111\}$ final facets, the $\{111\}A$ facets grow as growth times proceeds [Fig. 7(d.i)]. However, in the overgrowths displaying the perfect flat facets, the growth happens entirely on a single $\{110\}$ surface [Fig. 7(d.ii)]. The evolution of the InP and InGaAs layers is more clearly illustrated in Fig. S8 in the SM [25]. Figure 7(d.ii) also clearly demonstrates that lateral heterojunctions with flat facets are achievable.

Growing in templates oriented along [100] orientation yields a mixture of flat (001) facets and $\{111\}B$ facets

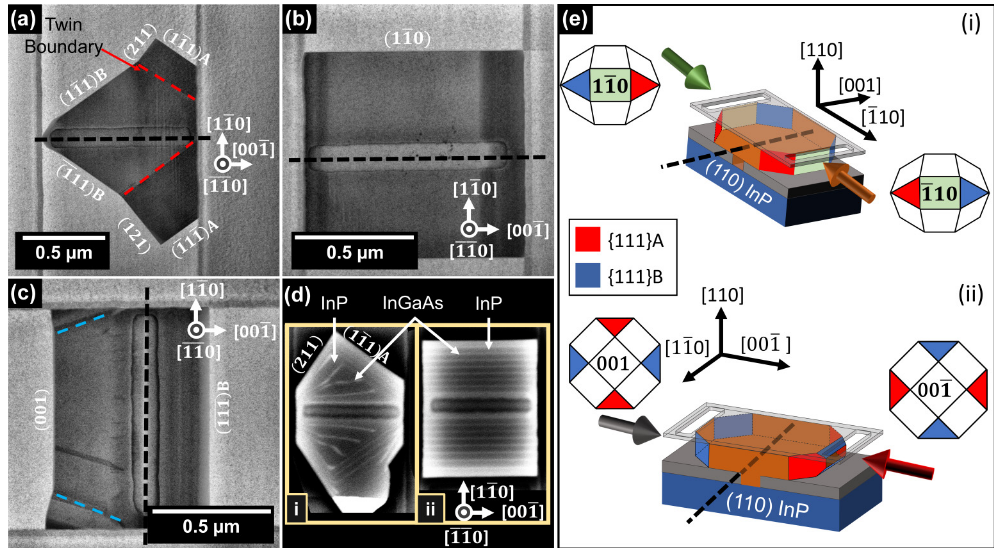

FIG. 7. Plan-view TEM of InP CELO grown on InP(110) substrates. (a), (b) show representative growths in templates oriented along $[1\bar{1}0]$. (a) shows twinning along the $\{111\}A$ planes (red dashed line); (b) shows perfect sharp $\{110\}$ type vertical flat facets. (c) shows CELO growth in templates oriented along [100]. The growth towards $\langle 100\rangle$ orientation is terminated by a sharp $\{100\}$ facet while the $\langle 00\bar{1}\rangle$ orientation is terminated by $\{111\}B$ facets. There are edge twins on the side growing towards $\langle 001\rangle$. Twin planes are marked by blue dashed lines. (d) shows backscatter SEM of two different growths in templates oriented along [110]. The bright lines are InGaAs markers in between InP growths. (e) shows how the crystal facets on the growth plane are different depending on which orientation the crystal grows in. The red and blue planes represent the $\{111\}A$ and $\{111\}B$ planes, respectively. The Miller cubes shown correspond to how it would look when viewed along the corresponding arrows.

[Fig. 7(c)]. The directions $\langle 00\bar{1}\rangle$ and $\langle 001\rangle$ offer different crystallographic planes for growth, resulting in different end facets for the growth in a single template [Fig. 7(e)]. Here, the growth front has two $\{111\}B$ top and bottom planes and two other $\{111\}A$ side planes when looking along $\langle 00\bar{1}\rangle$. The A and B planes get interchanged when viewing along $\langle 001\rangle$ Growths towards $\langle 00\bar{1}\rangle$ are mostly terminated by $\{111\}B$ type facets and form stacking faults [along blue $\{111\}B$ planes in Fig. 7(e.ii)]. The growths on the other side of the seed hole (towards $\langle 001\rangle$) are terminated by flat (001) type vertical facets perpendicular to the template, sometimes accompanied by small higher-order side facets, such as $\{211\}$. The growths towards $\langle 001\rangle$ are relatively defect free, with a few occasional stacking faults at the edges and small twins at the corner edges [blue dashed lines in Fig. 7(c)].

Thus, we demonstrate that on a (110) InP substrate, defect-free CELO overgrowths with vertical flat facets can be achieved in templates aligned along $[\bar{1}10]$. The perpendicular templates along [001] also form nanostructures with flat $\{001\}$ facets on one end, which can also find use in fabricating lateral heterojunctions.

IV. DISCUSSION

A. Facets

We observe that in CELO overgrowths on a (100) InP substrate growth, temperature and V/III ratio control the final facet shapes of the nanostructures (Figs. 2 and 5). At high growth temperature ($T > 600\,^{\circ}$C), $\{110\}$ and $\{111\}$ facets form, while at temperatures below 570 °C, primarily $\{111\}B$ facets form (Fig. 2). Similar tuning of facet ratios is achieved by changing the group-V/group-III flux ratios at 570 °C (Fig. 5). Collectively, these results suggest that the facet ratios are controlled by the effective phosphorus overpressure (chemical potential) on the facets, which, in turn, can be changed by both temperature and V/III ratio.

Changing surface reconstructions on different facets changes their surface energies and growth rates. Density functional theory and other first principle calculations predict that, for a $\{111\}B$ surface of InP, a high phosphorus overpressure will form P trimers, resulting in a (2×2) surface reconstruction [30–32]. Similar As trimer formation has been previously reported on GaAs epitaxial lateral overgrowth [33–35]. These stable P trimers significantly suppress the growth rate on the $\{111\}B$ planes, as they block sites for the attachment of the incoming In atoms/trimethylindium molecules [36]. This reduces the effective indium incorporation coefficient on the $\{111\}B$ surface, resulting in the growth rate of other surfaces, such as the $\{110\}$ surfaces, dominating the growth. The $\{111\}B$ thus becomes the slowest growing and dominant surviving facet of the structure [37] for highly effective group-V overpressure (high V/III or low-temperature growth condition). However, at lower effective phosphorus overpressure (achieved either by higher growth temperature or low V/III flux ratio), large $\{110\}$ type facets and smaller $\{111\}B$ facets are formed. This arises from the effective V/III ratio decreasing and the (2×2) P trimer surface reconstruction becomes less favorable resulting in an In-rich $(\sqrt{3} \times \sqrt{3})$ surface becoming more stable [31]. This increases the In incorporation ratio and hence, the growth rate on the $\{111\}B$ surface. Therefore for (100) substrates, V/III ratio and growth temperature can control the ratio of $\{110\}$ and $\{111\}B$ surface areas in the CELO nanostructures. This offers tunability of

facets and shapes of selective area grown nanostructures to fabricate nanoscale devices with desired geometries.

Despite achieving this control over tuning facet ratios, the dominating final facets in CELO grown on (100) substrates are a combination of {110} and {111}*B*. This limits the use of these nanostructures for horizontal heterojunctions, for lack of flat single facets perpendicular to the lateral direction of growth. To achieve such flat lateral perpendicular facets, we explored a (110) InP substrate, where in a template aligned along [$\bar{1}$10], {111}*B* planes are absent in the direction of growth. This provides an opportunity to form flat perpendicular facets in the direction of growth. A large number of the growths in these templates, however, show twinned crystal growths [Fig. 7(a)]. From the InGaAs marker layer growths [Fig 7(d.i)], we assume that a small {111}*A* facet was formed in the overgrowth immediately after it extended out of the seed hole. As the growth proceeded, more precursor materials diffuse to the {110} facet from the {111}*A* surface (which has a lower growth rate). The nonuniform diffusion causes the {110} surface to grow thicker on the side closer to the {111}*A* facet, thus forming a slanted growth front. As the growth proceeds further, the {110} is completely transformed to a {112}*B* and then the growth proceeds primarily on the {111}*A* surface. The growth can stop on a {111}*B* instead of a {112}*B* giving rise to the facets seen in Fig. 7(a).

However, when the {111} facet does not form at the start, the crystal can grow entirely on the {110} surface. This results in completely flat and vertical {110} facets [Fig. 7(b)]. The InGaAs markers included in the growth confirm this growth evolution [Fig. 7(d.ii)]. A critical factor in achieving these facets is the suppression of the {111}*A* facet as the material grows out of the seed hole. This process is assumed to be affected partly by the roughness of the dielectric sidewalls, as explained in the "Defects" section below. Hence, we have demonstrated that the [$\bar{1}$10] oriented templates on a (110) InP substrate can form flat vertical facet surfaces, which is one of the main requirements in building horizontal lateral heterojunctions and superlattices with flat interfaces.

Templates oriented along the [001] orientation also produce flat {001} facets on one end of the nanostructures [Fig. 7(c)]. This is of key interest because the ⟨001⟩ orientation of a CELO template oriented along [100] might offer another favorable direction to achieve lateral heterojunctions.

The results of this study can be carried over to other III-V CELO growth systems. Although the III-V nucleation on other mismatched substrates (such as Si) is different from homoepitaxy, once the epitaxial layer starts growing out on top of the oxide template, the same growth mechanism and facet dependencies on temperature and V/III ratio should apply.

B. Defects

Growth temperature and V/III ratios play a significant role in changing defect type and density in CELO grown nanostructures on a (100) InP substrate. At lower temperatures or high V/III ratios during growth, the growth along the {111}*B* planes is suppressed and growth proceeds more on the {110} surfaces. This growth suppression lowers the number of planar defects that form on the {111} planes (Figs. 2 and 5). The trapezoidal shape of the stacking faults arises from the interference fringes from one or more closely located stacking faults [38]. Low-temperature or high V/III ratio growth also exhibits stacking faults bound by partial dislocations [39] and incomplete stacking fault pyramidal loops. These defects are known to be generated by various stress mechanisms induced by thermal expansion coefficient mismatch [40]. This suggests that roughness or thermal expansion mismatch induced stress from the CELO oxide sidewalls might lead to these defects.

At higher growth temperature or lower V/III ratio, the increased growth rate on the {111}*B* surfaces favors the formation of bands of stacking faults and twins along the growth front. These planar defects are aligned along the {111}*B* plane, consistent with the fact that the {111} plane is the primary twinning plane for III-V semiconductors [16,22]. At high temperatures, isolated stacking faults do not appear. This is possibly because the defects are more mobile at elevated temperatures, enabling them to spread to the edges of the nanostructures.

Many of the defects appear to be generated from interaction of the growing III-V material with the rough sidewalls of the template (Fig. 5). In a confined system such as CELO, the roughness of the inner sidewalls of the template can play a significant role in defect formation. Interaction of the III-V crystal with a rough oxide has been reported to cause bond distortions in GaAs, leading to formation of twins and stacking faults [41]. In our case, we hypothesize that etching-induced roughness of the oxide sidewalls (of both the seed and template) contributes to the formation of stacking faults. In addition, it must be noted that the thermal expansion coefficient for InP is $\alpha = 4.6 \times 10^{-6}\,^{\circ}\mathrm{C}^{-1}$ while that of SiO_2 is $\alpha = 0.5 \times 10^{-6}\,^{\circ}\mathrm{C}^{-1}$. This large thermal expansion mismatch will result in stress in the InP epitaxial lateral overgrowth upon cooling after growth [42–47]. The highest stress appears at the edges of the oxide template, which is likely to result in stacking faults and twins starting at the edge of the dielectric [43]. While high V/III ratios during growth lower the defect densities in the overgrown template farther away from the seed hole, no considerable changes in the defect densities near the seed hole were observed (Fig. 5). A detailed study to decouple the effects of local growth parameters, oxide roughness, and thermal expansion mismatch in defect generation is beyond the scope of this paper.

We observe that the orientation of the templates impacts the defect densities. On InP(100), growths in the templates oriented along the [001] direction [Fig. 6(b)] show regions with the largest area of defect-free overgrown crystal. This result agrees with the study by Staudinger *et al.* [16]. The growth in the [001] orientation is free of any {111} planes along the direction of growth, thus reducing the formation of stacking faults. The growths, however, show the formation of stacking faults along the side facets, which contain {111} planes. As the direction of the template changes from being oriented along [001] [Fig. 6(b)] to being directed along [110] [Fig. 6(e)], the growth front has a higher percentage of {111} planes. As a result, we see stacking faults increase and the areas of defect-free crystal decrease. The interaction of III-V materials with a SiO_2 surface contributes to the formation of the stacking faults, as mentioned above. Therefore, we demonstrate that overgrowths with larger areas in contact with the sidewalls will show a higher number of defects (Fig. 6).

On a (110) InP substrate, if the growth occurs primarily on the {110} surfaces, the likelihood of forming twinning or stacking faults is lower compared to growth on the {111} surfaces. Thus, in $[\bar{1}10]$ oriented templates on a (110) substrate, when a higher fraction of the growth front is along $[\bar{1}10]$ a relatively defect-free crystal forms. Subsequently, after twin formation, when growth proceeds primarily on a {111} surface, stacking faults appear [Fig. 7(a)]. Such stacking faults also appear in growths along $\langle 00\bar{1}\rangle$ where the growth front consists of {111}*B* surfaces. If, however, the growth proceeds entirely on the {110} surface, no defects appear in the entire structure [Fig. 7(b)]. Such defect-free nanostructures with perpendicular flat facets can enable the fabrication of high-quality lateral heterojunction devices. Similarly, growths in the $\langle 001\rangle$ have very few stacking faults, as growth happens primarily on the {001} surface. By choosing template orientations, we can effectively lower the defect densities for nanostructures grown on a (110) substrate.

It should be noted here that, in addition to the CELO-induced defects observed in this study, for heteroepitaxial III-V CELO growth on mismatched substrates (such as Si), additional dislocations, stacking faults, and antiphase boundaries will result from lattice and symmetry mismatch. Although the oxide template beside the seed hole should in principle trap most of these defects, it is not always guaranteed and often they can spread into the overgrown epitaxial layer.

V. CONCLUSION

In conclusion, we demonstrate that for homoepitaxial InP CELO on InP substrates, the facets, defect types, and defect densities all depend heavily on the growth conditions, such as temperature, V/III ratio, template orientation, and InP substrate orientation. For (100) InP substrates, high growth temperature (or low V/III ratio) results in nanostructures with a combination of {110} and {111}*B* type facets. Conversely, for low growth temperature (or high V/III ratio), {111}*B* end facets dominate. We attribute this dependence on temperature and V/III ratios to surface energies and formation of phosphorus trimers in phosphorus-rich environments suppressing growth on the {111}*B* plane. We also show that low growth temperature (or high V/III ratio) and alignment of templates along [010] together can give very low defect densities on a (100) InP substrate. To achieve vertical facets critical for growing lateral heterojunctions, we utilize templates aligned along $[1\bar{1}0]$ on a (110) InP substrate. With these templates, we demonstrate nearly defect-free and perfectly vertical {110} type facets, with a single growth front – making them promising for the formation of lateral heterojunctions with flat vertical interfaces. Our results show the ability to grow CELO nanostructures with well-controlled facets. This will widen applications of CELO for fabricating quantum-well based devices, where orientations of the quantum wells are crucial for harnessing the benefits of orientation dependent carrier confinement and mobility. In addition, using growth conditions, substrate orientations, and template alignments we can reduce defects in these nanostructures, potentially leading to low leakage currents in devices and enhanced electronic and optical performances.

ACKNOWLEDGMENTS

This research is funded by the National Science Foundation (NSF) (Grant No. 1640030) and by the Semiconductor Research Corporation (Grant No. 2016-EP-2694-A), and made use of shared facilities of the UCSB MRSEC (NSF DMR 1720256) and the Nanotech UCSB Nanofabrication facility.

[1] J. Z. Huang, P. Long, M. Povolotskyi, G. Klimeck, and M. J. W. Rodwell, P-type tunnel FETs with triple heterojunctions, IEEE J. Electron Devices Soc. **4**, 410 (2016).

[2] J. Z. Huang, P. Long, M. Povolotskyi, H. Ilatikhameneh, A. Tarek, R. Rahman, and M. J. W. Rodwell, A multiscale modeling of triple-heterojunction tunneling FETs, IEEE Trans. Electron Devices **64**, 2728 (2017).

[3] W. Mizubayashi, S. Noda, Y. Ishikawa, T. Nishi, A. Kikuchi, H. Ota, P. H. Su, Y. Li, S. Samukawa, and K. Endo, Impacts of plasma-induced damage due to UV light irradiation during etching on Ge fin fabrication and device performance of Ge fin field-effect transistors, Appl. Phys. Express **10**, 026501 (2017).

[4] K. Eriguchi, Y. Takao, and K. Ono, A new aspect of plasma-induced physical damage in three-dimensional scaled structures—sidewall damage by stochastic straggling and sputtering, in *2014 IEEE International Conference on IC Design and Technology* (Institute of Electrical and Electronics Engineers, Piscataway, NJ, 2014), pp. 1–5.

[5] S. F. Fang, K. Adomi, S. Iyer, H. Morkoç, H. Zabel, C. Choi, and N. Otsuka, Gallium arsenide and other compound semiconductors on silicon, J. Appl. Phys. **68**, R31 (1990).

[6] H. Moriceau, F. Rieutord, F. Fournel, L. Y. Tiec, L. Di Cioccio, C. Morales, A. M. Charvet, and C. Deguet, Overview of recent direct wafer bonding advances and applications, Adv. Nat. Sci.: Nanosci. Nanotechnol. **1**, 043004 (2010).

[7] S. Mauthe, N. V. Triviño, Y. Baumgartner, M. Sousa, D. Caimi, T. Stöferle, H. Schmid, and K. E. Moselund, InP-on-Si optically pumped microdisk lasers via monolithic growth and wafer bonding, IEEE J. Sel. Top. Quantum Electron. **25**, 1 (2019).

[8] A. Ogura and Y. Fujimoto, Novel technique for Si epitaxial lateral overgrowth: Tunnel epitaxy, Appl. Phys. Lett. **55**, 2205 (1989).

[9] P. J. Schubert and G. W. Neudeck, Confined lateral selective epitaxial growth of silicon for device fabrication, IEEE Electron Device Lett. **11**, 181 (1990).

[10] H. Schmid, M. Borg, K. Moselund, L. Gignac, C. M. Breslin, J. Bruley, D. Cutaia, and H. Riel, Template-assisted selective epitaxy of III-V nanoscale devices for co-planar heterogeneous integration with Si, Appl. Phys. Lett. **106**, 233101 (2015).

[11] M. Borg, H. Schmid, K. E. Moselund, G. Signorello, Gignac, L. J. Bruley, C. Breslin, P. Das Kanungo, P. Werner, and H. Riel, Vertical III-V nanowire device integration on Si(100), Nano Lett. **14**, 1914 (2014).

[12] S. Mauthe, Monolithic integration of III-V on silicon for photonic and electronic applications, in *Proceedings of the 76th Device Research Conference (DRC), Santa Barbara, CA*

(Institute of Electrical and Electronic Engineers, Piscataway, NJ, 2018), pp. 1–2.

[13] M. Borg, H. Schmid, K. E. Moselund, D. Cutaia, and H. Riel, Mechanisms of template-assisted selective epitaxy of InAs nanowires on Si, J. Appl. Phys. **117**, 144303 (2015).

[14] M. Knoedler, N. Bologna, H. Schmid, M. Borg, K. E. Moselund, S. Wirths, M. D. Rossell, and H. Riel, Observation of twin-free GaAs nanowire growth using template-assisted selective epitaxy, Cryst. Growth Des. **17**, 6297 (2017).

[15] L. Czornomaz, E. Uccelli, M. Sousa, V. Deshpande, V. Djara, D. Caimi, M. D. Rossell, R. Erni, and J. Fompeyrine, Confined epitaxial lateral overgrowth (CELO): A novel concept for scalable integration of CMOS-compatible InGaAs-on-insulator MOSFETs on large-area Si substrates, in *2015 Symposium on VLSI Technology* (Institute of Electrical and Electronics Engineers, Piscataway, NJ, 2015), pp. T172–T173.

[16] P. Staudinger, S. Mauthe, K. E. Moselund, and H. Schmid, Concurrent zinc-blende and wurtzite film formation by selection of confined growth planes, Nano Lett. **18**, 7856 (2018).

[17] D. Cutaia, K. E. Moselund, H. Schmid, M. Borg, A. Olziersky, and H. Riel, Complementary III-V heterojunction lateral NW tunnel FET technology on Si, in *2016 Symposium VLSI Technology* (Institute of Electrical and Electronic Engineers, Piscataway, NJ, 2016).

[18] C. Convertino, C. Zota, H. Schmid, D. Caimi, M. Sousa, K. Moselund, and L. Czornomaz, InGaAs FinFETs directly integrated on silicon by selective growth in oxide cavities, Materials **12**, 87 (2019).

[19] S. Wirths, B. F. Mayer, H. Schmid, M. Sousa, J. Gooth, H. Riel, and K. E. Moselund, Room-temperature lasing from monolithically integrated GaAs microdisks on silicon, ACS Nano **12**, 2169 (2018).

[20] S. T. Šuran Brunelli, A. Goswami, B. Markman, H. Y. Tseng, M. Rodwell, C. Palmstrøm, and J. Klamkin, Horizontal heterojunction integration via template-assisted selective epitaxy, Cryst. Growth Des. **19**, 7030 (2019).

[21] P. Long, J. Z. Huang, M. Povolotskyi, D. Verreck, J. Charles, T. Kubis, G. Klimeck, M. J. W. Rodwell, and B. H. Calhoun, A tunnel FET design for high-current, 120 mV operation, in *International Electron Devices Meeting, IEDM* (Institute of Electrical and Electronics Engineers, Piscataway, NJ, 2017), pp. 30.2.1–30.2.4.

[22] H. A. Fonseka, P. Caroff, J. Wong-Leung, A. S. Ameruddin, H. H. Tan, and C. Jagadish, Nanowires grown on InP (100): Growth directions, facets, crystal structures, and relative yield control, ACS Nano **8**, 6945 (2014).

[23] H. Gottschalk, G. Patzer, and H. Alexander, Stacking fault energy and ionicity of cubic III–V compounds, Phys. Status Solidi **45**, 207 (1978).

[24] M. O. Manasreh, InP and related compounds materials, applications and devices, *Optoelectronic Properties of Semiconductors and Superlattices Vol. 9* (CRC Press, Boca Raton, FL, 2000).

[25] See Supplemental Material at http://link.aps.org/supplemental/10.1103/PhysRevMaterials.4.123403 for (S1) lamella preparation methods; (S2) TEM analysis of CELO growth at high temperature; (S3) slanted cross-section TEM of high temperature grown CELO; (S4) total growth area comparisons at different temperatures and V/III ratios; (S5) plan-view BF STEM in two-beam conditions; (S6) color marked backscatter SEM of InP CELO with InGaAs spacer layers; (S7) CELO template fabrication process steps (see also Ref. [48]).

[26] L. A. Giannuzzi and F. A. Stevie, A review of focused ion beam milling techniques for TEM specimen preparation, Micron **30**, 197 (1999).

[27] C. Li, G. Habler, L. C. Baldwin, and R. Abart, An improved FIB sample preparation technique for site-specific plan-view specimens: A new cutting geometry, Ultramicroscopy **184**, 310 (2018).

[28] C. J. Humphreys, Fundamental concepts of stem imaging, Ultramicroscopy **7**, 7 (1981).

[29] P. J. Phillips, M. J. Mills, and M. De Graef, Systematic row and zone axis STEM defect image simulations, Philos. Mag. **91**, 2081 (2011).

[30] H. Shu, X. Chen, X. Zhou, Z. Ding, and W. Lu, First-principles study of initial growth of InP nanowires: Self-catalytic effect and nucleation mechanism of in adatoms, J. Phys. Chem. C **114**, 10195 (2010).

[31] H. Shu, X. Chen, R. Dong, X. Wang, and W. Lu, Thermodynamic phase diagram for hydrogen on polar InP(111)B surfaces, J. Appl. Phys. **107**, 063516 (2010).

[32] E. Pehlke and M. Scheffler, Equilibrium shapes and energies of coherent strained InP islands, Phys. Rev. B **60**, 17008 (1999).

[33] D. K. Biegelsen, R. D. Bringans, J. E. Northrup, and L.-E. Swartz, Reconstructions of GaAs ($\bar{1}\bar{1}\bar{1}$) Surfaces Observed by Scanning Tunneling Microscopy, Phys. Rev. Lett. **65**, 452 (1990).

[34] H. Paetzelt, V. Gottschalch, J. Bauer, G. Benndorf, and G. Wagner, Selective-area growth of GaAs and InAs nanowires—homo- and heteroepitaxy using SiN_x templates, J. Cryst. Growth **310**, 5093 (2008).

[35] K. Nakamura, T. Mano, M. Oshima, H. W. Yeom, and K. Ono, High-resolution core-level photoemission study on GaAs (111) B surfaces, J. Appl. Phys. **101**, 043516 (2007).

[36] H. J. Chu, T. W. Yeh, L. Stewart, and P. D. Dapkus, Wurtzite InP nanowire arrays grown by selective area MOCVD, Phys. Status Solidi C **7**, 2494 (2010).

[37] N. Julian, P. Mages, C. Zhang, J. Zhang, S. Kraemer, S. Stemmer, S. Denbaars, L. Coldren, P. Petroff, and J. Bowers, Coalescence of InP epitaxial lateral overgrowth by MOVPE with V/III ratio variation, J. Electron. Mater. **41**, 845 (2012).

[38] D. Hull and D. J. Bacon, *Introduction to Dislocations* (Elsevier, Amsterdam, 2011).

[39] C. Frigeri, R. Gleichmann, C. Pelosi, and G. Attolini, Relationship between dislocation generation, vapour phase supersaturation and growth rate in InP layers obtained by vapour phase epitaxy, Mater. Sci. Eng. B **10**, 197 (1991).

[40] G. Salviati, C. Ferrari, L. Lazzarini, L. Nasi, A. V. Drigo, M. Berti, D. De Salvador, M. Natali, and M. Mazzer, Structural characterization of InGaAs/InP heterostructures grown under compressive and tensile stress, Appl. Surf. Sci. **188**, 36 (2002).

[41] C. Renard, N. Cherkasin, A. Jaffre, L. Vincent, A. Michel, T. Molière, R. Hamouche, V. Yam, J. Alvarez, F. Fossard, D. Mencaraglia, and D. Bouchier, Dislocation and antiphase domain free microscale GaAs crystals grown on SiO_2 from (001) Si nano-areas, Appl. Phys. Lett. **102**, 191915 (2013).

[42] M. E. Groenet, Monolithic heteroepitaxial integration of III-V semiconductor lasers on Si substrates, Ph.D. thesis, Massachusetts Institute of Technology, 2002.

[43] S. Ghosh, D. Leonhardt, and S. M. Han, Experimental and theoretical investigation of thermal stress relief during epitaxial growth of Ge on Si using air-gapped SiO_2 nanotemplates, Appl. Phys. Lett. **99**, 181911 (2011).

[44] T. Fujii, T. Sato, K. Takeda, K. Hasebe, T. Kakitsuka, and S. Matsuo, Epitaxial growth of InP to bury directly bonded thin active layer on SiO_2/Si substrate for fabricating distributed feedback lasers on silicon, IET Optoelectron. **9**, 151 (2015).

[45] W. Ju, D. A. Gulino, and R. Higgins, Epitaxial lateral overgrowth of gallium nitride on silicon substrate, J. Cryst. Growth **263**, 30 (2004).

[46] P. M. J. Marée, J. C. Barbour, J. F. Van Der Veen, K. L. Kavanagh, C. W. T. Bulle-Lieuwma, and M. P. A. Viegers, Generation of misfit dislocations in semiconductors, J. Appl. Phys. **62**, 4413 (1987).

[47] J. Selvidge, J. Norman, E. T. Hughes, C. Shang, D. Jung, A. A. Taylor, M. J. Kennedy, R. Herrick, J. E. Bowers, and K. Mukherjee, Defect filtering for thermal expansion induced dislocations in III-V lasers on silicon, Appl. Phys. Lett. **117**, 122101 (2020).

[48] S. T. Šuran Brunelli, B. Markman, A. Goswami, H. Y. Tseng, S. Choi, C. Palmstrøm, M. Rodwell, and J. Klamkin, Selective and confined epitaxial growth development for novel nano-scale electronic and photonic device structures, J. Appl. Phys. **126**, 015703 (2019).